Effects of Microfabrication Processing on the Electrochemistry of Carbon Nanofiber Electrodes

**Timothy E. McKnight,*,† Anatoli V. Melechko,†,‡ Michael A. Guillorn,†,§
Vladimir I. Merkulov,† Mitchel J. Doktycz,∥ Christopher T. Culbertson,⊥ Stephen C. Jacobson,#
Douglas H. Lowndes,@ and Michael L. Simpson†,§**

Oak Ridge National Laboratory, Oak Ridge, Tennessee 37831

Received: April 3, 2003; In Final Form: July 4, 2003

We describe the fabrication and electrochemical characterization of as-grown and postprocessed vertically aligned carbon nanofiber forest electrodes at macroscopic (5 mm) and microscopic dimensions (250 μm). We examine the impact of a variety of microfabrication processes that are typically employed during nanofiber-based device synthesis including refractory metal reactive ion etch, oxide coating and removal, and several oxygen-based etch processes—all of which dramatically impact microscale electrode response. We also demonstrate that the high electrochemically active surface area of larger scale, macroscopic nanofiber forest electrodes can provide a buffering capacity against surface activation/inactivation. Under diffusion-limited transport conditions, this may preserve the electrochemical response of the electrode during storage and against the impacts of processing techniques used during nanofiber-based device fabrication.

Introduction

Motivation. Vertically aligned carbon nanofibers (VACNF) are self-assembling, catalytically synthesized structures that span across multiple length scales, featuring nanoscale tip radii (20–50 nm) and lengths up to tens of microns. When combined with the ability to direct nanofiber synthesis with a high level of determinism[1,2] VACNFs can provide a bridge between molecular-scale phenomena and the macroscopic world, thereby enabling the realization of truly functional nanoscale devices including nanomanipulators, field-emitters,[3] fluidic pipes,[4] cellular-scale material delivery vectors,[5] and individually addressable electrochemical sensors[6] that may be functionalized for specific analytes, including DNA.[7] Previously, we described that single VACNFs could be synthesized on electrical interconnects and implemented as individual electrochemical electrodes where only the extreme nanoscale tip of the fiber was electrochemically active.[6] The nanofiber served both to elevate the electroanalytical measurement volume above the planar substrate and to electrically bridge between the nanoscale dimensions of the fiber tip and the microscale dimensions of the electrical interconnects of the substrate. Here, we explore the integration of VACNFs as electrochemical components of *larger* electrode systems, including microfabricated (250 μm) band electrodes and larger scale (5 mm) forests of aligned fibers. We also address the electrochemical impact of a variety of processing techniques that are employed during nanofiber-based device microfabrication.

* Corresponding author. E-mail: mcknightte@ornl.gov.
† Molecular-Scale Engineering and Nanoscale Technologies Research Group.
‡ Department of Electrical and Computer Engineering, University of Tennessee, Knoxville, TN 37996.
§ Department of Material Science and Engineering, University of Tennessee, Knoxville, TN 37996.
∥ Life Science Division.
⊥ Department of Chemistry, Kansas State University, Manhattan, KS 66506.
@ Condensed Matter Sciences Division.
# Chemical Sciences Division.

Carbon Electrodes. Carbon electrodes are one of the most thoroughly studied electrochemical materials. In general, carbon-based electrodes feature relatively wide potential windows in aqueous media, are low cost, have low chemical and electrochemical reactivity, and provide reproducible responses following appropriate surface treatments. There are several excellent reviews of the electrochemical performance of various conventional carbon-based electrode systems, with glassy carbon, carbon paste, (highly ordered) pyrolytic, and (wax-impregnated) graphite serving as some of the more common embodiments.[8,9] At the largest size scale, low-cost electrode materials such as graphite are often employed for industrial-scale electrochemical processes, such as aluminum manufacture. Micro- and ultramicroelectrodes, typically employing either bundles of bulk carbon nanotubes produced via catalytic chemical vapor deposition or graphitic carbon produced by heat treatment of polymeric precursors, are often the method of choice for small-volume, in vivo electrochemical analyses.[10,11] Each of these forms of carbon has unique properties, with wide variations between the different types with respect to reactivity, adsorption phenomena, and surface group coverage that ultimately affect electrochemical performance. Carbon nanofibers, as individual elements or in large arrays, provide the opportunity to produce carbon-based electrode systems over a wide range of size scales from nanoelectrodes to large, wafer-scale areas. However, even among the group of materials termed "nanofibers", there is a wide variety of synthesis techniques and likely similar variation in the mechanical, electrical, and electrochemical performance of the resultant structures.

The VACNFs we employ in our work are synthesized in a dc-plasma enhanced chemical vapor deposition process, involving the catalytic decomposition of acetylene on nickel and explained in detail by Merkulov et al.[12] Unlike single and multiwalled carbon nanotubes, nanofibers are not hollow concentric graphene cylinders but rather have morphologies ranging from cylindrical to conical with internal caps within an otherwise hollow core.[13] *Vertically aligned* refers to the parallel orientation

Device Processing Effects on Nanofiber Electrochemistry

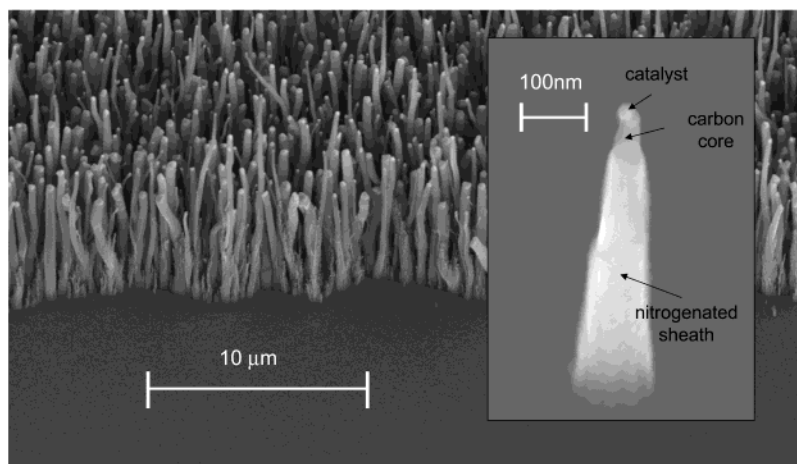*J. Phys. Chem. B, Vol. 107, No. 39, 2003* **10723**

Figure 1. Scanning electron micrographs of a densely populated nanofiber forest and an isolated carbon nanofiber (inset) imaged at a 30° viewing angle. The isolated specimen features a highly ordered carbon core and a nitrogenated sheath. This morphology of sheathed fibers is typical, with the sheathing material extending only partially up the length of the fiber.

(normal to the substrate) of *tip-grown* nanofibers, where the nickel catalyst particle precipitates dissolved carbon from the decomposed acetylene precursor on its lower surface.[2] As carbon is precipitated in highly ordered form beneath the catalyst particle, the catalyst is elevated above the substrate and remains resident on the fiber tip as the fiber grows. In transmission electron micrographs, the resultant nanofiber exhibits a herringbone-like structural cross section with grain boundaries of graphitic planes running parallel with the faceted lower faces of the nickel catalyst in a stacked funnel configuration.

Patterned VACNF Synthesis. The site of fiber growth is determined by definition of a thin film of nickel catalyst, typically 200−1000 Å thick. Prior to fiber growth, a brief thermal/NH_3 plasma process is used to break up the nickel film and nucleate it into isolated nanoparticles, each of which will initiate growth of a single fiber. Nickel nucleation will vary on the basis of the interaction of the nickel solution with the underlying substrate and often a buffering layer of titanium is employed to aid in catalyst nucleation. As a point of reference, upon silicon or titanium, single catalyst particles can typically be nucleated from 100 Å thick nickel dots that are less than 100 nm in diameter.[1] These defined catalyst dots can be patterned by lift-off techniques following electron-beam or deep-UV lithography. Larger area nickel films at this thickness will nucleate multiple particles and will thus catalyze densely packed, randomly spaced fibers arrays, which we refer to as nanofiber *forests* (Figure 1). Several electrochemical studies have been conducted on structures somewhat similar to these forests, including thermal CVD grown fibers using a nickel- or iron-based catalyst[14] and thermal CVD structures termed "multi-walled carbon nanotube towers" grown using Fe as catalyst.[15] These latter structures feature vertically aligned properties similar to PECVD grown fibers, but the alignment mechanism is believed to be due to steric crowding on the substrate.[12] Bulk addressed, sparse nanoelectrode arrays featuring isolated individual fibers defined from disperse electrodeposited nickel catalysts have also been documented.[16]

An important aspect of nanofiber synthesis with respect to electrochemistry is that in addition to deposition of carbon through the nickel catalyst, species generated in the plasma will also deposit as a film on the sheath and tip of the fiber and, to a lesser extent, upon the substrate between fibers. Ammonia is employed throughout the growth process to continuously remove this film from the fiber tip as it will passivate the catalytic surface of the nickel particle and stop growth.[17] Variation of

synthesis parameters, particularly the acetylene/ammonia ratio, enables selection of the amount of film allowed to remain on the fiber sheath as a covering of the carbon core. The chemical composition of this film can be tailored from essentially pure carbon to carbon heavily doped with nitrogen (up to 70% surface content according to electron dispersive X-ray (EDX) analysis[12]). Figure 1 (inset) is an electron micrograph of an isolated nanofiber with a nitrogen-rich film sheath and a tip that is predominantly carbon except for an encased nickel catalyst particle. The composition of the sheathing film likely impacts the electrochemical performance of fibers. For example, nitrogen-incorporated carbon films can exhibit higher resistivity and reduced electron-transfer kinetics when compared to carbon films.[18] In this SEM image, the resistive nitrogenated sheath film can be visualized by the marked color contrast with the darker, conductive carbon core. The surface film also affects surface adsorption and physicochemical phenomena, including hydrophobicity, of the final structure. Forests of carbon rich fibers exhibit some hydrophobicity immediately following growth whereas nitrogenated films exhibit reduced hydrophobicity with increasing nitrogen content. The extent of hydrophobicity is difficult to quantify, however, as capillary wicking of analyte into the forest matrix still occurs after a few moments of contact even on markedly hydrophobic forests. Nonetheless, this variation in the wetting properties of the electrode material may be a factor with respect to analyte approach to interfiber spaces. In this work, we focus only on electrochemistry of fibers with negligible nitrogen content.

Results and Discussion

Fabrication of Macroscale Nanofiber Forest Electrodes. Large area electrodes of nanofiber forests were fabricated as multiple 1 cm × 3 cm stripes on N-type silicon wafers. Clean 3 in. wafers were patterned with these stripes by successive evaporative physical vapor depositions of 500 Å of titanium and 500 Å of nickel using a shadow mask to define the electrode patterns. Following metallization, dc-PECVD fiber synthesis was conducted resulting in nanofiber forest-covered electrodes with negligible nitrogen content (<1% via EDX analysis). Synthesis time was 60 min, resulting in fibers of approximately 5 μm length, relatively cylindrical aspect ratio, and 100 nm average diameter. Nanofiber density within the forests was approximately 10^6 nanofibers/mm². Following fiber growth and inspection using scanning electron microscopy and electron dispersive
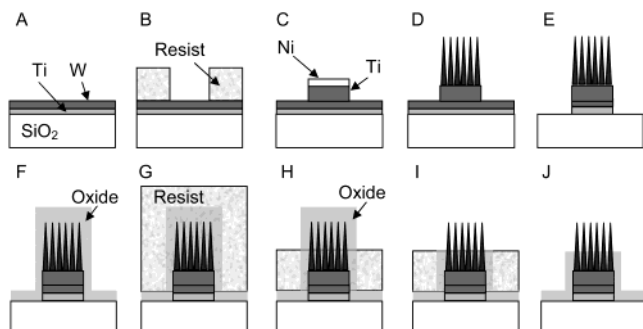
Figure 2. Fabrication process for patterning of fiber forest electrodes (A)−(E), and subsequent oxide partial passivation of these electrodes (F)−(J). Individual processing steps are described in the text. Note, components of figures are not drawn to scale.

X-ray elemental analysis, 5 mm diameter reservoirs were epoxied to multiple locations upon the forested stripe to define a fixed geometric surface area for subsequent electroanalysis. SEM imaging was used to confirm that the epoxy fixative did not substantially wick into the forested electrode region within the reservoir.

Fabrication of Patterned Forests of Nanofibers on Discrete Electrodes. The process for fabricating patterned microelectrodes of nanofiber forests is outlined in Figure 2. The substrates used for these electrodes were fused silica microscope slides measuring 7.5 cm by 2.5 cm and 1 mm thick. Slides were ultrasonically cleaned in acetone and rinsed with methanol and Nanopure water. A 100 Å layer of titanium followed by 100 Å of tungsten was deposited on the entire top surface of the slide, using electron gun physical vapor deposition at 10^{-6} Torr (Figure 2a). This thin layer of tungsten provides a conductive surface on nonconductive substrates and is required to remove charge buildup on such substrates during PECVD nanofiber growth. Electrode patterns were then defined on top of this tungsten layer with a lift-off technique. In brief, slides were spun with photoresist (Shipley 1813) and the positive image of the desired electrode patterns was exposed. Development (Shipley CD26) resulted in removal of the resist in the electrode pattern. The slide was then metallized with 400 Å of titanium followed by 100 Å of nickel, using electron-gun physical vapor deposition. Excess, nonelectrode metallization was lifted off by soaking and agitating the substrate in acetone for 1 h, followed by rinsing in a spray of acetone, isopropyl alcohol, and Nanopure water. The resultant pattern was a thick layer of titanium, capped with nickel in the patterned areas, on top of a uniform thinner layer of tungsten/titanium covering the entire substrate (Figure 2c).

Fiber growth was conducted using dc-PECVD as previously described (Figure 2d). Although fibers could be defined at discrete locations of electrodes using an additional lithographic step for discrete nickel deposition, fibers were grown over the entire length of these electrodes, including the interconnects and bonding pad areas. The electrode pattern was composed of electrode stripes of 250 micron width at 250 micron intervals across the slide. Following fiber growth, isolation of individual electrodes was achieved by removing the thin, tungsten/titanium layer on the substrate with a 10 min refractory metal reactive ion etch. (Refractory metal reactive ion etch parameters: 100 mTorr pressure, 115 W RF, 20 sccm SF_6, 3 sccm O_2, 40 sccm CF_4.) During this etch, the fiber forests upon the thicker metallized leads served as a mask for the underlying metal, whereas the thinner, unprotected metal in nonfibered areas was removed (Figure 2e). Slides were inspected with scanning electron microscopy and EDX.

Several of the 250 micron wide electrode samples were partially passivated using a technique presented in earlier work.[6] In brief, following fiber growth these electrode samples were conformally coated with 100 nm of PECVD silicon dioxide (Figure 2f). Bonding pad areas were kept free of oxide by covering them with polyimide tape prior to PECVD oxide deposition. The polyimide tape was removed following oxide deposition. The samples were then buried in spun-on photoresist (Shipley 1813) (Figure 2g) and subjected to an oxygen reactive ion etch (oxygen RIE parameters: TRION etcher, 350 mTorr pressure, 150 W RF, 50 sccm O_2) to remove enough of the resist to expose the tops of the silicon dioxide coated fibers (Figure 2h). A silicon dioxide-removing reactive ion etch (oxide RIE parameters: TRION etcher, 200 mTorr pressure, 200 W RF, 7 sccm O_2, 75 sccm CHF_3) was then used to emancipate the carbon nanofiber tips from the oxide coating (Figure 2i). Following tip emancipation, photoresist was removed by soaking in acetone for 1 h, followed by spraying with acetone, isopropyl alcohol, and distilled water. Resultant structures featured approximately 5 micron long emancipated carbon nanofiber tips on top of 1 micron of oxide-coated bases and oxide-coated interconnect structures (Figure 2j). Electrode structures were electrochemically analyzed without any postsynthesis processing and with this partial oxide passivation treatment. Additionally, to observe the effects of postsynthesis processing, samples of the larger electrode structures (3 cm × 1 cm stripes) were subjected to individual processing techniques, including oxygen reactive ion etch, oxide reactive ion etch, refractory metal reactive ion etch, and photoresist spin-on and removal.

Electrochemical Characterization. The various electrode configurations were evaluated using a variety of outer sphere, quasireversible analytes including $K_4Fe(CN)_6$ and $Ru(NH_3)_6$-Cl_3 at 0.5, 1, and 5 mM concentrations in 100 mM KCl. Electroanalysis was performed in a shielded faraday cage with a commercially available three-wire potentiostat (Model CH660A, CH Instruments, Austin, TX) using a Ag|AgCl in 3 M KCl reference electrode and a large surface area coiled platinum counter electrode. Electrical interconnects were made to all electrodes through the top surface of the electrodes, in an adjacent area outside of the fluid reservoirs.

Figure 3a and b provides representative cyclic voltammograms (CV; 100 mV/s) for 0, 1, and 5 mM solutions of potassium ferrocyanide and ruthenium hexamine trichloride in 0.1 M KCl for large surface area (5 mm diameter) carbon nanofiber forest electrodes synthesized with negligible nitrogen content. These electrodes were subjected to no additional processing treatments following their synthesis, including no specific chemical/thermal/or mechanical activation procedures. Even without "activation", however, the quasi-reversible $Fe(CN)_6^{3-}$/$Fe(CN)_6^{4-}$ and the $Ru(NH_3)_6^{3+}$/$Ru(NH_3)_6^{2+}$ couples exhibit fast electron-transfer kinetics, with cathodic and anodic peak separation very near the ideal 59 mV for a single electron-transfer reaction, and the anodic/cathodic peak ratio near unity. Note, to achieve these voltammograms, resistive drop (IR) compensation was employed. Without IR compensation, peak shifts of up to 30 mV would be observed for the higher concentrations of analyte due to cumulative solution/electrode/interconnect resistive drop (approximately 100 Ω of total resistance). It is particularly interesting to note that these voltammograms were obtained approximately 5 months following electrode synthesis. During this period, no restrictive storage procedures were used except mechanical protection in a closed, polypropylene 3 in. wafer container. The nanofiber forest electrodes were thus
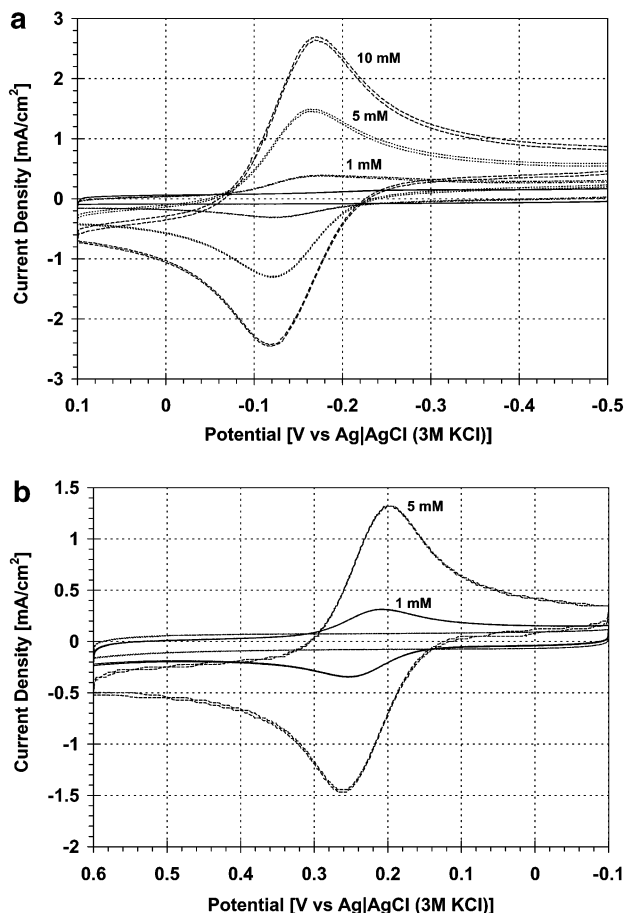
Device Processing Effects on Nanofiber Electrochemistry

J. Phys. Chem. B, Vol. 107, No. 39, 2003 **10725**

Figure 4. Voltammograms of 250 μm wide stripe electrodes without additional processing ("as grown") and following a partial oxide passivation process, where the lower portion of the fiber forest and interconnect structure is coated with 100 nm of PECVD silicon dioxide per steps (F)−(J) in Figure 2.

Figure 3. Responses of 5-mm diameter nanofiber forest electrodes to varying concentrations of (a) ruthenium hexamine trichloride and (b) potassium ferrocyanide. These voltammograms are IR compensated to account for resistive losses in the interconnect/fiber−substrate junction/solution, which are pronounced due to the relatively large currents from the high-concentration analytes. All subsequent voltammograms are not IR compensated.

exposed to air and subject to the accumulation of airborne contaminants.

Evaluation of the CVs in Figure 3 indicates diffusion-limited electrode responses, but with peak currents approximately 10−15% greater than that expected from a 5 mm diameter planar electrode where analyte access is limited to the electrode surface by semi-infinite planar diffusion.[19] As discussed elsewhere,[15,20] the additional charge transferred can be explained by redox of the analyte adsorbed to and within the free volume of the "porous" electrode matrix. A rough estimation of the analyte volume within the recesses of our 5 mm diameter, 5 μm tall nanofiber forest electrodes is approximately 100 nL. This analyte volume would result in an equivalent of 10 μC of charge transfer for a 1 mM solution of ruthenium hexammine trichloride, which is is approximately 10% of the total charge transferred in the 1 mM CV wave for $Ru(NH_3)_6^{3+}$ reduction.

Electrode capacitances of the 5 mm diameter electrodes were determined by observing capacitance current at 0 mV vs Ag|AgCl (3 M) during CV in 100 mM KCl at scan rates of 100, 200, 400, 800, and 1600 mV/s and resulted in 560 ± 50 μF/cm^2 ($n = 3$) based upon a geometric surface area of 0.2 cm^2. This capacitance is dramatically higher than that expected from a planar carbon electrode of the same geometric surface area (20−100 μF/cm^2)[8] due to the large increase in surface area provided by the vertical orientation of the individual fiber elements of the forest. Estimates indicate that the microscopic
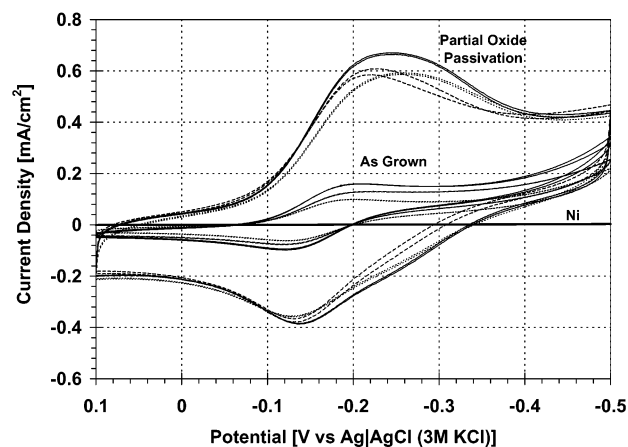
surface area is approximately a factor of 10 greater than the projected geometric surface area of 0.2 cm^2 for these electrodes. These data support that these macroscale electrodes operate in an extreme diffusion-limited regime, where the actual surface area is approximately 10 times larger than that required for analyte redox under semi-infinite planar diffusion-limited conditions. This excess surface area may compensate for the inactivation of some of the surface area that likely occurs during storage and provides a potential explanation for why these electrodes do not require specific electrode activation. The heterogeneity along the length of individual nanofibers within a nanofiber forest, as presented in Figure 1, may also help maintain an active surface area, as each region of the fiber is likely affected (inactivated) differently by adsorption of surface contaminants.

Figure 4 presents the cyclic voltammograms (CV, 100 mV/s) for 1 mM ruthenium hexamine trichloride in 100 mM KCl for three separate 250 μm wide, 5 mm long nanofiber electrodes before (steps a−e of Figure 2) and after partial oxide passivation processing (steps f−j of Figure 2). Similar to the 5 mm diameter fiber forests, the carbon nanofibers of these electrodes have negligible nitrogen content as measured by EDX elemental analysis. For reference, the response of an unfibered, nickel electrode with identical footprint is provided, indicating that there should be little redox activity of any nickel catalyst that may be exposed in the samples.

On the basis of a geometric surface area of 0.0125 cm^2, the unpassivated (bare) fiber stripes had current density maxima of 0.16 mA/cm^2 for the 1 mM cathodic wave, which is less than the expected diffusion-limited flux to the electrode if fully activitated. It is possible that the additional processing involved in the fabrication of these microscale electrodes, specifically a refractory metal reactive ion etch, may have deactivated some of the electrode surface. For example, metallic oxides may sputter during this process and cover some of the active surface area of the fibered stripe. In contrast, following the processing steps involved with partial passivation, which includes an oxygen plasma etch of oxide coated fibers and a subsequent oxide etch removal of this oxide coating, the current density of partially passivated electrodes increased by approximately a factor of 4 to 0.6−0.7 mA/cm^2.

As the partial passivation process *reduces* the overall exposed nanofiber surface area with an oxide covering, it is interesting that the partially oxide coated fibers had significantly *higher* anodic (I_{pa}) and cathodic peak currents (I_{pc}) than those uncoated

with oxide. After subtraction of the baseline current, which also is increased for the oxide coated fibers, these fibers exhibit approximately 3-fold increase in I_{pc} and I_{pa}. A variety of factors may be responsible for the overall increased currents. The oxide coating and etching process increases the hydrophilicity of the surface and therefore may improve wetting of and therefore analyte access to larger fiber surface areas. The various reactive ion etch processes used during photoresist and oxide removal can also be responsible for removing many passivating surface contaminants that might be present on fibers, including those that may have been generated during the refractory metal reactive ion etch used to define the microscale electrode pattern. Thus, though the *apparent* surface area of the fibers has been decreased by the oxide coating on the lower sheaths of the fibers, the *actual* active surface area may be increased due to this improved analyte access and removal of surface contaminants. Increased surface area could also result in the observed increased background currents due to increased area for double layer capacitance. Additionally, "pseudocapacitance" could also be increased in the oxide processed samples, resulting from faradaic reactions of surface oxides generated on the fibers from energetic oxygen radicals during oxide etching.

In addition to peak current increases, it would appear that the cathodic peak is broadened in the oxide processed fibers with respect to bare fibers. Though this gives the initial impression that the anodic and cathodic peak separation (ΔE_p) is increased and the kinetics of the $Ru(NH_3)_6^{2+}/Ru(NH_3)_6^{3+}$ couple are reduced, on closer inspection, the peak broadening of the cathodic wave is found to actually be due to the presence of a second reduction wave at -300 mV vs Ag|AgCl (3 M KCl). For the 250 μm wide nanofibered stripes, this reduction wave is not present in the background voltammograms of neat 100 mM KCl and appears to have originated during $Ru(NH_3)_6^{3+}/Ru(NH_3)_6^{2+}$ analyses. The -300 mV reduction wave, however, does persist in background voltammograms following the $Ru(NH_3)_6^{3+}/Ru(NH_3)_6^{2+}$ analyses and after thorough rinsing of the electrode with distilled water. As such, the new reduction wave may be due to complexation of ruthenium compounds with surface oxides that were generated during the etch processes. However, this reduction wave is also close in potential to a similar peak that was observed during capacitance calculations for the 5 mm large area electrodes which were unexposed to ruthenium (data not shown). Therefore, this wave may be due to an existing surface oxide whose activity was increased during the ruthenium electroanalyses. For this electrode, background subtraction of this -300 mV peak effectively eliminates the apparent peak broadening seen in Figure 4, indicating that no significant increase in ΔE_p results from oxide processing of fibers for the ruthenium hexamine trichloride system. This is consistent with many published reports of the insensitivity of the outer-sphere $Ru(NH_3)_6^{3+}/Ru(NH_3)_6^{2+}$ couple to surface oxides.[8]

To isolate which processing step of oxide coating/removal is affecting nanofiber electrochemistry, samples with bare 250 μm wide nanofiber electrodes were exposed to independent single processing steps. During fabrication, these patterned, fiber electrode stripes were subjected to a refractory metal reactive ion etch, to remove interelectrode metallization (tungsten) and thus isolate individual electrode stripes. During the partial passivation process, fibers were further subjected to an oxide coating, resist exposure, a polymer etch (oxygen RIE), and an oxide etch (oxygen/CHF$_3$ RIE). As oxygen-based techniques are frequently cited as methods to improve carbon electrode activation, we subjected 250 μm wide fibered electrodes to 1
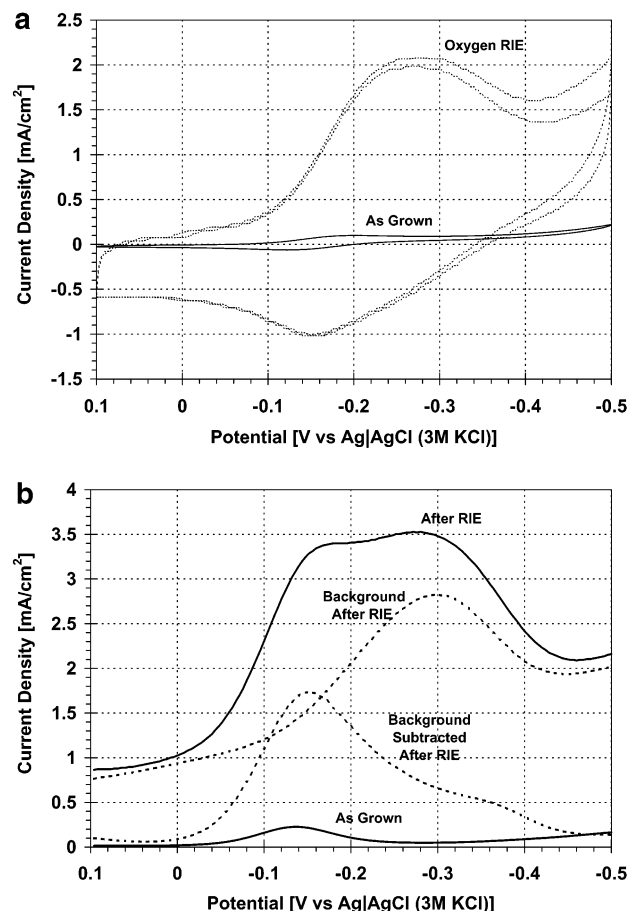

Figure 5. (a) Cyclic voltammogram of 1 mM ruthenium hexamine trichloride on a 250 μm wide fiber forest before and after a 1 min oxygen reactive ion etch. The oxygen RIE dramatically increases the capacitance and peak heights of the 250 μm fibered stripe. (b) Differential pulse voltammograms of an unprocessed and 1 min oxygen RIE treated fiber stripe. A new cathodic peak is observed following oxygen RIE at -300 mV. Background subtraction of this peak, and the background capacitive current, provides a DPV similar to the untreated forest electrode, but significantly greater in magnitude (5×).

min exposures to the oxygen reactive ion etch process. This oxygen RIE processing had a significant impact on fiber electrode electrochemistry, similar to, but greater than, that seen in Figure 4 for fully processed, partially oxide-coated fibers. Figure 5a presents the CV of a bare fiber stripe electrode (as grown), and the same electrode after 1 min of oxygen RIE. Similar to the partially passivated samples, dramatic increases in peak heights can be observed as well as increases in the capacitive background and the apparent stretching of the cathodic peak which is actually due to the generation of a new reduction wave at -300 mV vs Ag|AgCl (3 M KCl). Figure 5b presents the differential pulse voltammograms (DPV) for the $Ru(NH_3)_6^{2+}/Ru(NH_3)_6^{3+}$ couple on an unprocessed, bare fiber, 250 μm wide electrode stripe, and for such a stripe following 1 min of oxygen RIE. Also shown is the background DPV in 100 mM KCl and the background-subtracted DPV for $Ru(NH_3)_6^{3+}$. As can be observed, the background-subtracted DPV does overlay the bare fiber DPV, eliminating the reduction wave at -300 mV vs Ag|AgCl (3 M), but an increase in current density by a factor of 5 is still observed due to the oxygen RIE treatment.

Additional individual processing treatments were conducted on as-grown, larger area, 5 mm diameter carbon fiber forest electrodes; including direct exposure to resist (Shipley 1813), a 5 min oxygen plasma reactive ion etch, and a 10 min refractory
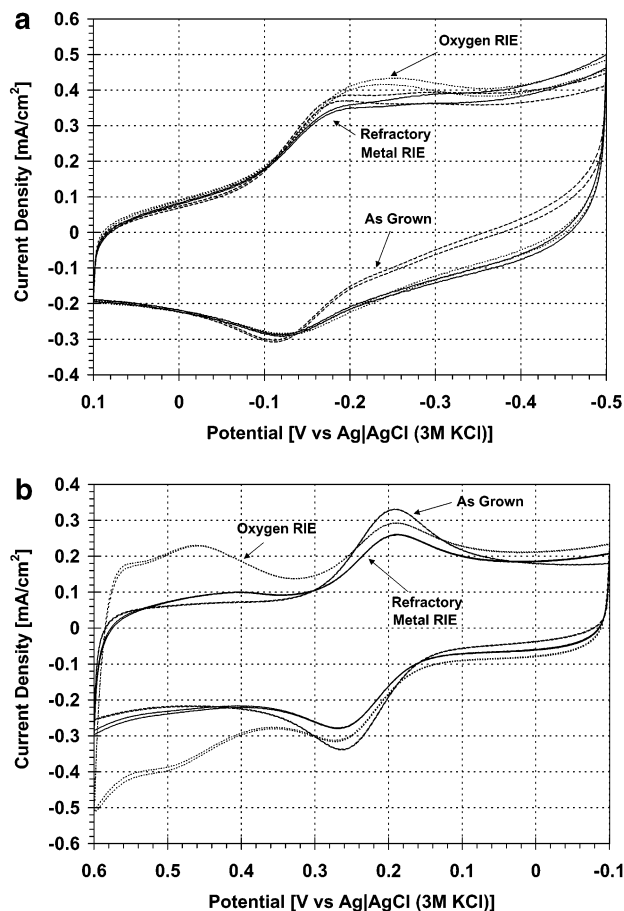
Device Processing Effects on Nanofiber Electrochemistry

J. Phys. Chem. B, Vol. 107, No. 39, 2003 **10727**

Figure 6. (a) Responses of large area (5 mm diameter) nanofiber forest electrodes to 1 mM ruthenium hexamine trichloride following synthesis (as grown), refractory metal RIE, and oxygen RIE. (b) Responses to 1 mM potassium ferrocyanide. The oxygen RIE sample indicates several additional new redox peaks at potentials >400 mV vs Ag|AgCl (3 M). In general, however, neither processing effect dramatically impacts these large surface area electrodes as they did for the 250 μm stripe electrodes.

metal etch. Although these processing effects did impact the electrochemical performance of these larger electrodes, these effects were considerably less pronounced than those observed on the 250 μm wide electrode patterns and were not consistent across the samples. Figure 6a presents the CV of 1 mM ruthenium hexamine trichloride on an unprocessed 5 mm diameter electrode (as grown), a refractory metal etched electrode, and an electrode exposed to a 5 min oxygen reactive ion etch. In each of these CVs, the broadened cathodic peak is observed due to the extraneous peak at −300 mV vs Ag|AgCl (3 M), even on the as grown sample, which experienced no additional processing following synthesis. In sharp contrast to what was observed on 250 μm wide electrodes, however, these etch treatments did not consistently affect the resultant electrode electrochemistry on 5 mm diameter electrodes. Across 5 samples, there was no consistent increase or decrease in electrode capacitance, I_{pa} and I_{pc}, and no significant shift in ΔE_p. Figure 6b presents a sample of as grown/oxygen-etched/refractory-etched electrode responses to 1 mM potassium ferrocyanide. Again, no dramatic and no consistent increases or decreases in peak height resulted and electron kinetics are slightly changed from sample to sample, but not consistently. Significant new peaks are observed, however, in all oxygen RIE samples ($n >$ 15 samples) at several potentials greater than 400 mV vs Ag|AgCl (3 M). For example, in Figure 6b, one of these new peaks is evident at 500/440 mV.

The results presented above demonstrate that processing effects, particularly exposure to energetic oxygen radicals, resulted in significant activation of patterned 250 μm wide electrodes but had considerably less effect upon the responses of larger, unpatterned electrode surface areas. This may relate to the inability to significantly chemically alter the deep recesses of the large electrode forests, in contrast to the 250 μm stripes that have similar deep forests but also feature large surfaces that are exposed to processing effects on each side of the fibered stripe. Further, though the 250 μm wide electrode forests will experience some radial diffusion of analyte to each side of the fibered stripe, the large surface areas of the 5 mm diameter electrodes appear to place these electrodes under extreme semi-infinite planar diffusion limits. As such, alterations in the electrochemical activity due to passivation during storage or processing effects during device fabrication may have less influence on electrode response. Perhaps the changes that these alterations impart are not significant enough to move the electrode system out of semi-infinite planar diffusion limits. To better observe the effects of these treatments, however, further studies using techniques that move the system out of this diffusion-limited regime (such as rotating disk and other hydrodynamic methods) are necessary.

Conclusion

Deterministically synthesized vertically aligned carbon nanofibers provide the means to realize electrochemical electrodes over a wide range of size scales, from nanoscale individual elements to large, wafer-scale, forests. Although the latter may typically be produced with little need for patterning, the incorporation of nanofibers as components in functional microscale and nanoscale devices will inevitably involve a variety of processing steps including various etch techniques, coating processes, and photolithographic patterning. Although we provide data that indicate that, at a microscale, these processing effects can have a dramatic impact on nanofiber electrode chemistry, we also show that, for diffusion-limited macroscale electrodes, the surface area enhancement afforded by the high-aspect ratio morphology of vertically aligned carbon nanofiber forests may serve as a buffer to these same processing effects, including exposure to resist, oxygen reactive ion etching, and refractory metal etch processes. This same buffering capacity also may be beneficial for preserving performance of nanofiber electrodes temporally, minimizing the need for activation procedures required for many conventional forms of carbon electrodes. The surface heterogeneity of nanofibers, resulting from the catalytic nature of highly ordered carbon nanofiber growth and an independent deposition of carbonaceous (and/or nitrogenated) film onto the fiber, may also provide unique advantages with respect to electrode application and stability.

References and Notes

(1) Merkulov, V. I.; Lowndes, D. H.; Wei, Y. Y.; Eres, G.; Voelkl, E. Patterned growth of individual and multiple vertically aligned carbon nanofibers. *Appl. Phys. Lett.* **2000**, *76* (24), 3555.

(2) Merkulov, V. I.; Melechko, A. V.; Guillorn, M. A.; Lowndes, D. H.; Simpson, M. L. Alignment mechanism of carbon nanofibers produced by plasma- enhanced chemical-vapor deposition. *Appl. Phys. Lett.* **2001**, *79* (18), 2970.

(3) Guillorn, M. A.; Melechko, A. V.; Merkulov, V. I.; Ellis, E. D.; Simpson, M. L.; Baylor. L. R.; Bordonaro. G. J. Microfabricated field emission devices using carbon nanofibers as cathode elements. *J. Vac. Sci. Technol. B* **2001**, *19* (6), 2598.

(4) Melechko, A. V.; McKnight, T. E.; Guillorn, M. A.; Merkulov, V. I.; Lowndes, D. H.; Simpson, M. L. Nanopipe fabrication using vertically aligned carbon nanofiber templates. *J. Vac. Sci. Technol. B* **2002**, *20* (6), 2730.

(5) McKnight, T. E.; Melechko, A. V.; Griffin, G. D.; Guillorn, M. A.; Merkulov, V. I.; Serna, F.; Hensley, D. K.; Doktycz, M. J.; Lowndes, D. H.; Simpson, M. L. Intracellular integration of synthetic nanostructures with viable cells for controlled biochemical manipulation. *Nanotechnology* **2003**, *14* (5), 551.

(6) Guillorn, M. A.; McKnight, T. E.; Melechko, A. V.; Merkulov, V. I.; Britt, P. F.; Austin, D. W.; Lowndes, D. H.; Simpson, M. L. Individually addressable vertically aligned carbon nanofiber-based electrochemical probes. *J. Appl. Phys.* **2002**, *91* (6), 3824.

(7) Li, J.; Hou T. N.; Cassell, A.; Fan, W.; Chen, H.; Ye, Q.; Koehne, J.; Han, J.; Meyyappan, M. Carbon nanotube nanoelectrode array for ultrasensitive DNA detection. *Nano Lett.* **2003**, *3* (5), 597.

(8) McCreery, R. L. Carbon Electrodes: Structural Effects on Electron-Transfer Kinetics. *Electroanalytical Chemistry*; Bard, A. J., Ed.; Marcel Dekker: New York, 1991; Vol. 17.

(9) Kinoshita, K. *Carbon: Electrochemical and Physicochemical Properties*; Wiley: New York, 1988.

(10) Wightman, R. M.; Wipf, D. O. Voltammetry at ultramicroelectrodes. *Electroanal Chem.* **1989**, *15*, 267.

(11) Clark, R. A.; Zerby, S. E.; Ewing, A. G. *Electrochemistry in neuronal microenvironments, Electroanalytical Chemistry*; Bard, A. J., Ed.; Marcel Dekker: New York, 1998; Vol 20.

(12) Merkulov, V. I.; Hensley, D. K.; Melechko, A. V.; Guillorn, M. A.; Lowndes, D. H.; Simpson, M. L. Control mechanisms for the growth of isolated vertically aligned carbon nanofibers. *J. Phys. Chem. B* **2002**, *106* (41), 10570.

(13) Baker, R. T. K. Catalytic growth of carbon filaments. *Carbon* **1989**, *27* (3), 315.

(14) Shui, X.; Frysz, C. A.; Chung, D. D. L. Electrochemical behavior of hairy carbons. *Carbon* **1997**, *35* (10), 1439.

(15) Li, J.; Cassell, A.; Delzeit, L.; Han, J.; Meyyappan, M. Novel three-dimensional electrodes: electrochemical properties of carbon nanotube ensembles. *J. Phys. Chem. B* **2002**, *106*, 9299.

(16) Tu, Y.; Lin, Yuehe; Ren, Z. F. Nanoelectrode arrays based on low site density aligned carbon nanotubes. *Nano Lett.* **2003**, *3* (1), 107.

(17) Melechko, A. V.; Merkulov, V. I.; Guillorn, M. A.; Lowndes, D. H.; Simpson, M. L. Transition between 'base' and 'tip' carbon nanofiber growth modes. *Chem. Phys. Lett.* **2002**, *356* (5−6), 527.

(18) Cachet, H.; Deslouis, C.; Chouiki, M.; Saidani, B.; Conway, N. M. J.; Godet, C. Electrochemistry of nitrogen-incorporated hydrogenated amorphous carbon films. *J. Electrochem. Soc.* **2002**, *149* (7), E233.

(19) Bard, A. J.; Faulker, L. R. *Electrochemical methods: Fundamentals and Applications*; John Wiley and Sons: New York, 2001.

(20) Murphy, M. A.; Wilcox, G. D.; Dahm, R. H.; Marken, F. Adsorption and redox processes at carbon nanofiber electrodes grown onto a ceramic fiber backbone. *Electrochem. Commun.* **2003**, *5*, 51.